

Rigorous Modeling of Droplet Impact Dynamics on Micro-Structured Surfaces: Nonlocal Theory and SPH Simulation of Pancake Bouncing

Zhonghua Qiao ^{*} Zuankai Wang [†] Yifan Wei [‡]

September 3, 2025

Abstract

The accurate mathematical modeling of droplet impact dynamics on micro-structured surfaces is fundamental to understanding and predicting complex fluid behaviors relevant to a wide range of engineering and scientific applications. In particular, the pancake bouncing phenomenon—systematically studied by Liu et al. (*Nature Physics*, 2014)—on superhydrophobic micro-structured substrates presents significant theoretical challenges. Central to these challenges is the need to construct rigorous mathematical models that capture the intricate influence of substrate micro/nanostructures on droplet dynamics. This requires the development of robust formulations for surface tension, contact line dynamics, and the interaction forces between fluid and solid structures. In this work, we formulate a nonlocal mathematical framework for the simulation of 3D pancake bouncing on superhydrophobic micro-cone arrays. The model incorporates intermolecular attractive forces to represent droplet surface tension, and

^{*}Department of Applied Mathematics, The Hong Kong Polytechnic University, Hung Hom, Kowloon, Hong Kong (zhonghua.qiao@polyu.edu.hk).

[†]Department of Mechanical Engineering, The Hong Kong Polytechnic University, Hung Hom, Kowloon, Hong Kong (zk.wang@polyu.edu.hk).

[‡]Corresponding author. Department of Applied Mathematics, The Hong Kong Polytechnic University, Hung Hom, Kowloon, Hong Kong (yi-fan.wei@polyu.edu.hk).

we provide a strict theoretical derivation linking these forces quantitatively to the macroscopic surface tension coefficient, thereby circumventing the reliance on empirical parameter tuning. The complex geometry of micro-cone arrays introduces fundamental difficulties in defining local normal directions for contact algorithms. To overcome this, we develop a nonlocal contact repulsion force model that governs fluid-solid interactions and ensures numerical stability under high Weber number conditions. Based on this mathematical foundation, we implement the model using smoothed particle hydrodynamics (SPH), enabling high-precision 3D simulations. Computational experiments, validated against empirical data, confirm the model's accuracy and robustness, while underscoring the key role of numerical simulation in elucidating droplet-microstructure interactions.

keywords: Pancake bouncing; SPH method; attractive forces; nonlocal contact repulsion

1 Introduction

Understanding and controlling droplet rebound dynamics is essential for advancing liquid manipulation technologies in various engineering applications. This phenomenon is particularly critical in applications such as combustion systems [1], inkjet printing [2], anti-icing surfaces [3], corrosion-resistant coatings [4] and self-cleaning materials [5]. Recent studies reveal that these technologies have broad applications across fields including aerospace, biomedicine, automotive engineering, and smart textiles [6]. While hydrophobic coatings facilitate droplet removal, achieving directional control and efficient shedding requires not only low surface energy but also carefully designed nanostructures with tailored surface chemistry [7]. At such nano-enhanced interfaces, pancake bouncing [8] emerges as a remarkable phenomenon: droplets impacting nanostructured superhydrophobic surfaces lift off immediately in a flattened state without retracting, reducing contact time by approximately 75% compared to conventional rebound. Precise liquid control is crucial for advanced functional surfaces and devices, necessitating deeper research into droplet rebound dynamics, especially given their significant implications in healthcare and electronics.

The dynamics of droplet rebound has garnered considerable scientific attention, driving a steady stream of key discoveries in interfacial science[9].

Early studies by [10] revealed that droplets on superhydrophobic surfaces in low-pressure environments can self-remove through spontaneous levitation and trampoline-like bouncing. Later, [11] later identified a superhydrophobic-like bouncing regime on thin liquid films, where the rebound dynamics were independent of the underlying substrate. Subsequent work by [12] introduced a facile method to fabricate hierarchical multilayered superhydrophobic surfaces for efficient droplet shedding. [13] further explored symmetry-breaking impacts, showing that ellipsoidal droplets reduce contact time and suppress rebound magnitude. Recent advances have significantly enhanced control over droplet rebound behavior through novel interfacial strategies. [14] proposed a 'golden section' design criterion to regulate rebound via structural spacing, challenging conventional approaches. [15] developed a leaf-inspired superhydrophobic cantilever for directional bouncing, while [16] reduced contact time by coating droplets with hydrophobic particles. Additionally, through the utilization of innovative tools, a deeper understanding of the underlying mechanisms has been achieved. In their study, [17] utilized high-speed infrared thermography and a three-dimensional transient heat conduction COMSOL model to accurately map the dynamic heat flux distribution during droplet impact on a cold superhydrophobic surface. [18] introduced a novel micro-controlled droplet generator capable of releasing two equally sized water droplets simultaneously on-demand, enabling the investigation of the behavior of two droplets on a dry substrate. [19] reported that controlled self-transport of bouncing droplets can be achieved with the assistance of ultra-smooth surfaces featuring wedge-shaped grooves. [20] uncovered molecular-scale wetting dynamics through in situ characterization, providing fresh insights into droplet-surface interactions. And [21] conducted a comprehensive numerically assisted analysis based on verifiable assumptions such as quasi-stationarities and small Reynolds/Peclet numbers.

Although experimental investigations provide critical observations, numerical modeling is essential for achieving fundamental physical understanding and enabling technological applications. In fact, despite extensive experimental investigations into droplet impact phenomena, the fundamental physics governing collisions with hydrophobic surfaces remains inadequately understood, as noted in literature [22]. On the contrary, numerical modeling offers unique insights into interfacial phenomena. For example, [23] conducted numerical simulations based on the Cahn-Hilliard-Navier-Stokes model to achieve a complete and quantitative study on the effects of interfacial tension when it becomes sufficiently low. Additionally, [24] simulated

buoyancy-driven bubble-wall interactions using an adaptive ALE method, capturing the interaction of a rising bubble with a solid wall. Furthermore, [25] investigated the head-on collision of unequal-size droplets of the same liquid on wetting surfaces using direct numerical simulations at different size ratios. Based on the Onsager variational principle, [20] presented a phenomenological model that reveals how the intrinsic material parameters of soft gels dictate phase-separation dynamics. Moreover, fabricating nanostructured substrates for droplet impact studies incurs significant costs, whereas numerical simulations provide a cost-efficient alternative for parametric studies and experimental design optimization. Within this framework, numerical simulations have become pivotal in impact dynamics research. The creation of high-fidelity computational models capable of capturing intricate interfacial processes is essential for both theoretical advancements and practical applications.

Smoothed Particle Hydrodynamics (SPH) method, as a mesh-free Lagrangian method, offers distinct advantages in simulating droplet rebound phenomena. In fact, droplet rebound typically involves large interfacial deformations and topological changes, presenting inherent difficulties for grid-based simulations. Traditional Eulerian approaches, such as the Lattice Boltzmann method (LBM), rely on multiphase domain discretization and phase-field method to accurately capture fluid interfaces. While LBM excels in modeling complex multi-phase flows, its application to gas-liquid systems with high density ratios demands non-trivial modifications to ensure numerical stability [26, 27, 28]. By contrast, SPH circumvents these limitations through its fully Lagrangian mesh-free formulation, eliminating the need for explicit gaseous-phase discretization altogether [29]. This intrinsic capability renders SPH particularly suited for investigating droplet interactions with hydrophobic surfaces. Other alternative particle-based approaches such as molecular dynamics (MD) and dissipative particle dynamics (DPD) suffer from severe scalability limitations in mesoscale droplet simulations due to their demanding resolution requirements and consequent computational overhead. The SPH method achieves an optimal balance between numerical resolution and computational efficiency. Notably, while SPH has seen extensive practical applications in recent years, its theoretical foundations have been progressively strengthened. Significant contributions include Du et al.'s mathematical analysis from a nonlocal perspective [30, 31] and Sun et al.'s stability analysis through an energy-based framework [32, 33, 34]. These theoretical advancements have collectively reinforced SPH's position

as a robust and well-validated methodology for droplet dynamics research.

Surface tension modeling constitutes a critical component of SPH simulation for droplet dynamics, and numerous significant studies have been conducted in this area. Distinct from phase-field methods that regulate interface motion through energy minimization, SPH implementations necessitate the explicit definition of forces acting on interface particles to control interfacial behavior. In reality, researchers have developed two principal methodological approaches. The first approach is the Continuous Surface Force (CSF) formulation [35], which implements a volumetric force at fluid interfaces through local curvature estimation. While this method maintains physical consistency, it demands careful handling of surface normal vectors and curvature calculations near interface regions [36, 37, 38]. Furthermore, this approach faces challenges in simulating droplet topological changes. The second approach involves the particle-particle interaction force (PIF) model [39, 40], which bypasses the need for normal vector and curvature calculations. This method demonstrates versatility in simulating solid-liquid interactions and solid wettability. Despite its practical effectiveness, the second approach dependence on empirically determined strength of the interparticle attraction [41], lacking strong theoretical foundations, constitutes a major limitation. Notice that surface tension emerges from interparticle attractive forces. Thus, when these attraction strengths are empirically predetermined, the resulting surface tension coefficients become inherently uncontrollable, frequently leading to physical inconsistencies. Therefore, developing a method that preserves theoretical consistency while ensuring conciseness and broad applicability has become critically important.

The contact algorithms is an another challenge for stable and precise SPH simulation, particularly for simulating droplet collisions on intricate arrays of microcones. The inherent complexity of droplet impact dynamics, characterized by multiscale solid-liquid interactions, creates escalating challenges for contact algorithm stability as the Weber number increases [42]. The traditional repulsive force algorithms [36, 37, 43], as a popular contact algorithm, require accurate surface normals \mathbf{n} and vertical distance d_p to surface. Specifically, the repulsive force $\mathbf{F}_i^{\text{rep}}$ on particle i satisfies the following relation:

$$\mathbf{F}_i^{\text{rep}} \propto \frac{2|d_0 - d_p|}{(\Delta t)^2} m_i \mathbf{n}_i, \quad (1)$$

where Δt is time step, m_i is particle mass and d_0 is contact threshold dis-

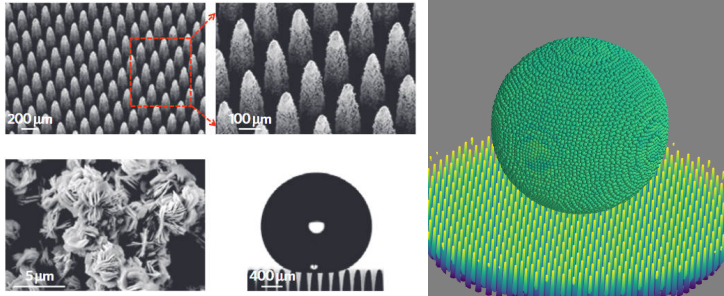


Figure 1: Droplet impact on microcone arrays: experimental observation (left; Copyright 2014 Springer Nature) and SPH simulation (right)

tance. Although this approach demonstrates satisfactory performance for ideally smooth substrates [9], its extension to realistically rough substrates encounters fundamental limitations. A representative case involves micro-structured hydrophobic surfaces [8], as illustrated in Fig. 1. In fact, due to the non-smoothness of the substrates, it is hard to determinate the local surface normals \mathbf{n}_i and vertical distance d_p . Besides, the virtual particle method is a widely used boundary treatment technique to address kernel truncation and wall penetration issues. However, when used in isolation, the virtual particle method often fails to reproduce physically accurate repulsive forces during droplet rebound. Consequently, the development of a robust contact algorithm capable of handling intricate microcone geometries is critical for reliable simulation of pancake bouncing dynamics.

The aim of this paper is to develop a robust and universally applicable numerical methods to capture pancake bouncing on superhydrophobic microcone arrays. In our work, the cohesive forces is introduce to simulate intermolecular attraction. Through theoretical derivation, we establish a relationship between cohesive forces and interfacial tension coefficients to ensure the physical consistency of the model. To address the contact issues of complex microcone structures, we define nonlocal contact repulsion in the boundary region to achieve stable simulation of pancake bouncing behavior in three-dimensional space. Our main contributions can be summarized as follows:

- (i) **A nonlocal mathematical framework** for droplet dynamics on micro-structured surfaces, rigorously linking intermolecular forces to the macroscopic surface tension coefficient without empirical parameter

tuning.

- (ii) **A stabilized nonlocal contact algorithm** for rough substrates, addressing the geometric challenges of micro-cone arrays by introducing a robust fluid-solid repulsion force model that ensures numerical stability at high Weber numbers.
- (iii) **High-fidelity SPH-based simulations** of pancake bouncing on superhydrophobic micro-cone arrays, validated against experimental data, which elucidate the role of microstructure interactions in droplet dynamics.

The rest of this paper is structured as follows. Section 2 presents the theoretical formulation of the governing equations for droplet impact dynamics. Section 3 develops a robust SPH discretization method. Section 4 provides comprehensive validation of the numerical model through systematic comparisons with experimental data. Finally, Section 5 summarizes the principal conclusions and their significance.

2 Governing equations

The bouncing dynamics of the droplet are governed by conservation equations of mass and momentum. The the Lagrangian-form of these equations can be expressed as:

$$\frac{d\rho}{dt} = -\rho \nabla \cdot \mathbf{u}, \quad (2)$$

$$\rho \frac{d\mathbf{u}}{dt} = -\nabla p + \mu \nabla^2 \mathbf{u} + \rho \mathbf{g} + \mathbf{f}_{\text{att}} + \mathbf{F}, \quad (3)$$

The governing equations involve the fluid velocity field \mathbf{u} , hydrodynamic pressure p , and local densities ρ . The pressure p is calculated by the following state of equation

$$p = \frac{c^2 \rho_0}{\gamma} \left(\left(\frac{\rho}{\rho_0} \right)^\gamma - 1 \right). \quad (4)$$

We adopt $\gamma = 7$ [44] for the equation of state, with ρ_0 and c denoting the reference densities and the numerical speed of sound, respectively. $\frac{d}{dt}$ represents the material derivative where $\frac{d}{dt} \equiv \frac{\partial}{\partial t} + \mathbf{u} \cdot \nabla$. μ denotes dynamic viscosity.

The body forces consist of gravitation $\rho\mathbf{g}$, droplet cohesive attractive force \mathbf{f}_{att} , and contact repulsion \mathbf{F} at the boundary interface.

Accurate characterization of cohesive attractive and repulsive interactions is crucial for reliably simulating droplet rebound dynamics on microcone arrays surfaces. In this section, we present a unified mathematical framework that integrates smoothed kernel functions with nonlocal operators to describe both \mathbf{f}_{att} and \mathbf{F} , enabling robust three-dimensional modeling of bouncing behavior.

2.1 Modeling of droplet cohesion

It is well-established that the surface tension of water droplets originates from intermolecular forces (hydrogen bonding and van der Waals interactions) between water molecules. While intermolecular interactions are physically straightforward, they impose prohibitive computational costs in macroscopic system simulations. For surface tension modeling at continuum scales, cohesive force models offer a viable alternative. For the simplicity of the mathematical representation, we need to introduce the smoothing kernel function $W(\mathbf{x} - \mathbf{x}', h)$, which satisfies the following conditions:

- Normalization condition: $\int_{\Omega} W(\mathbf{x} - \mathbf{x}', h) d\mathbf{x}' = 1$;
- Symmetric property: $W(\mathbf{x} - \mathbf{x}', h) = W(\mathbf{x}' - \mathbf{x}, h)$;
- Compact condition: $W(\mathbf{x} - \mathbf{x}', h) = 0$ where $|\mathbf{x} - \mathbf{x}'| \geq h$.

Here, $|\cdot|$ represents the Euclidean norm and h is the influence radius of kernel. $W(\mathbf{x}, h)$ affects only a specific support domain.

We now proceed to construct a cohesive forces model capable of generating physically accurate interfacial tension. In our work, each Lagrangian particle represents a finite fluid volume element comprising numerous water molecules. Between adjacent particles, we introduce an artificial cohesive force term $\mathbf{f}(\mathbf{x}, \mathbf{y})$ to approximate the net effect of microscopic intermolecular forces. Specifically, we denote the attraction of the particle at \mathbf{y} to the particle at \mathbf{x} as follows

$$\mathbf{f}(\mathbf{x}, \mathbf{y}) = A_{\sigma} \rho(\mathbf{y}) \nabla_{\mathbf{x}} W(\mathbf{x} - \mathbf{y}, R_1), \quad (5)$$

where A_{σ} is a parameter dependent on interfacial tension σ . The specific form of A_{σ} will be given later. $\nabla_{\mathbf{x}} W(\mathbf{x} - \mathbf{y}, R_1)$ in the same direction as

$\mathbf{y} - \mathbf{x}$. Thus, by integrating over \mathbf{y} , the total attractive force acting on the particle located at position \mathbf{x} is

$$\mathbf{f}_{\text{att}}(\mathbf{x}) = \int_{\Omega} \mathbf{f}(\mathbf{x}, \mathbf{y}) d\mathbf{y} = A_{\sigma} \int_{\Omega} \rho(\mathbf{y}) \nabla_{\mathbf{x}} W(\mathbf{x} - \mathbf{y}, R_1) d\mathbf{y}, \quad (6)$$

which implies that the attractive force scales with the nonlocal gradient of density.

The precise mathematical formulation of A_{σ} is of critical importance, as its rigorous definition serves as the foundation for ensuring both the algorithm's generalizability across diverse scenarios and its reliability in practical applications. Now we will establish a quantitative relationship between the parameter A_{σ} and surface tension σ through theoretical derivation. Notably, the droplet's curvature radius R is typically much larger than the cohesive force interaction radius R_1 . This scale separation justifies our model simplification that treats the liquid-gas interface as locally planar within the R_1 domain (i.e., $R \rightarrow \infty$ approximation). While this planar approximation introduces minor errors in the interaction integrals, the accuracy can be systematically improved by reducing R_1 through mesh refinement. Therefore, we can determine the relationship between A_{σ} and surface tension σ by studying the tension on a flat surface. Let ε denote the thickness of the surface. At any given point \mathbf{x}_0 on the surface, consider an arbitrary unit tangent vector \mathbf{t} at \mathbf{x}_0 . We use V_1 to describe the surface particles on one side of the normal plane of \mathbf{t} , and V_2 to denote all particles on the opposite side. Here, V_1 has a thickness of ε , while both V_1 and V_2 are strip-shaped regions of length L ($L \gg R_1$) (see Fig 2). Indeed, the precise relationship between

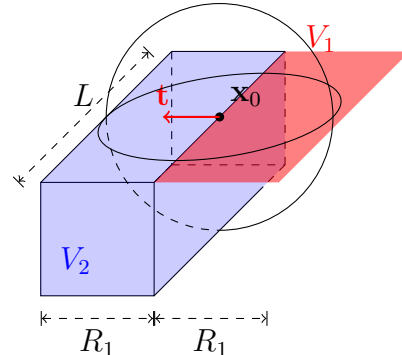


Figure 2: Schematic of cohesion at the gas-liquid contact surface

A_σ and σ can be formally established through the following theorem.

Theorem 1 (Effective surface tension generation) Consider a fluid domain Ω with constant density $\rho(\mathbf{x}) = \rho_0$ for all $\mathbf{x} \in \Omega$. Let \bar{f}_{att} denote the magnitude of the resultant attractive force along direction \mathbf{t} exerted by the fluid in region V_2 on the surface of V_1 , defined as

$$\bar{f}_{\text{att}} = \int_{V_1} \int_{V_2} [\mathbf{f}(\mathbf{x}, \mathbf{y}) \cdot \mathbf{t}]_+ d\mathbf{y} d\mathbf{x}, \quad (7)$$

where $[\cdot]_+$ denotes the positive part, and \mathbf{f} is the pairwise force given in (5). If the coefficient A_σ in the (5) takes the form

$$A_\sigma = \frac{4\sigma}{\rho_0 \varepsilon} \quad \text{such that} \quad \mathbf{f}(\mathbf{x}, \mathbf{y}) = \frac{4\sigma}{\rho_0 \varepsilon} \rho(\mathbf{y}) \nabla_{\mathbf{x}} W(\mathbf{x} - \mathbf{y}, R_1), \quad (8)$$

then the attractive force satisfies

$$\bar{f}_{\text{att}} = \sigma L. \quad (9)$$

This establishes that the cohesive force \mathbf{f} generates an effective fluid interface with surface tension coefficient σ .

Proof 1 Starting from the definition (7) and the artificial cohesive force (5), we obtain

$$\begin{aligned} \bar{f}_{\text{att}} &= A_\sigma \rho_0 \int_{V_1} \int_{V_2} [\nabla_{\mathbf{x}} W(\mathbf{x} - \mathbf{y}, R_1) \cdot \mathbf{t}]_+ d\mathbf{y} d\mathbf{x} \\ &= A_\sigma \rho_0 \int_{V_1} \int_{V_2} \left[f(|\mathbf{x} - \mathbf{y}|) \frac{\mathbf{x} - \mathbf{y}}{|\mathbf{x} - \mathbf{y}|} \cdot \mathbf{t} \right]_+ d\mathbf{y} d\mathbf{x}, \end{aligned} \quad (10)$$

where we used the relation $f(|\mathbf{x}|) = \partial_{|\mathbf{x}|} W(\mathbf{x}, R_1)$ and $\nabla_{\mathbf{x}} |\mathbf{x}| = \mathbf{x}/|\mathbf{x}|$.

Let θ be the angle between \mathbf{t} and $\mathbf{y} - \mathbf{x}$. The integrand simplifies to

$$\frac{\mathbf{x} - \mathbf{y}}{|\mathbf{x} - \mathbf{y}|} \cdot \mathbf{t} = -\cos \theta.$$

By exploiting the symmetry of V_1 , the volume integral of \mathbf{x} in (10) can be reduced to a line integral via $\mathbf{x} = \mathbf{x}_0 - s\mathbf{t}$. Furthermore, adopting spherical coordinates (r, θ, ϕ) centered at \mathbf{x} with the transformation

$$\mathbf{y} = \mathbf{x} + r \begin{pmatrix} -\cos \theta \\ \sin \theta \cos \phi \\ -\sin \theta \sin \phi \end{pmatrix} \quad \text{and} \quad r = |\mathbf{x} - \mathbf{y}|,$$

(10) can be reformulated as

$$\begin{aligned}\bar{f}_{\text{att}} &= -A_\sigma \rho_0 L \varepsilon \int_0^{R_1} \int_0^\pi \int_0^{\arccos(s/R_1)} \int_{s/\cos\theta}^{R_1} f(r) \cos\theta r^2 \sin\theta dr d\theta d\phi ds \\ &:= -A_\sigma \rho_0 L \varepsilon G_f,\end{aligned}\quad (11)$$

where G_f represents the quadruple integral expression. After careful evaluation of this integral (see Appendix A for detailed derivation), we obtain the simplified form

$$G_f = \frac{\pi}{3} \int_0^{R_1} f(r) r^3 dr. \quad (12)$$

Noting that $f(|\mathbf{x}|) = \partial_{|\mathbf{x}|} W(\mathbf{x}, h)$, where W is a kernel function, we can further evaluate this expression to yield

$$G_f = -\frac{1}{4}. \quad (13)$$

Substituting (13) into (11) gives the intermediate result

$$\bar{f}_{\text{att}} = \frac{\varepsilon L A_\sigma \rho_0}{4}. \quad (14)$$

Finally, by incorporating the expression for A_σ from (8) into (14), we arrive at the desired result (9).

The physical interpretation of this result follows directly from the definition of surface tension: the interfacial force per unit length between regions V_1 and V_2 is exactly $\bar{f}_{\text{att}}/L = \sigma$. This demonstrates conclusively that the pairwise cohesive force $\mathbf{f}(\mathbf{x}, \mathbf{y})$ defined in (8) generates an effective surface tension with coefficient σ at the interface between the fluid regions. This completes the proof.

Remark 1 Theorem 1 is established under the assumption of zero interface curvature. Nevertheless, this approach maintains reasonable accuracy with a mathematically verifiable relative error below 4.5% for scenarios where the radius of curvature is no less than R_1 . The relative error bound was confirmed through the selection of cubic spline kernel functions and numerical integration of Eq. (10). To avoid unnecessary computational complexity associated with curvature corrections, we retain the original cohesive force formulation (8) without modification.

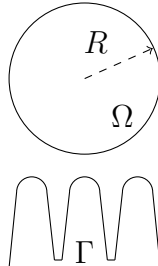


Figure 3: Schematic diagram of a droplet with a substrate

2.2 Modeling of substrate contact repulsion

The fluid-solid interaction poses significant computational challenges in particle-based simulations. While conventional no-penetration conditions suffice for macroscopic phenomena like dam-break flows, they become inadequate for microscopic interfacial processes such as droplet bouncing. This necessitates precise characterization of repulsive forces on fluid particles, particularly when dealing with geometrically complex boundaries.

Conventional contact algorithms typically require determining both the substrate's normal direction and the vertical distance to compute repulsive forces (using Equation (1)). However, this requirement becomes overly restrictive for substrates with complex geometries, such as the one illustrated in Figure 1. The method not only incurs substantial computational overhead but also demonstrates numerical instabilities, especially in concave regions where precise distance definition proves particularly challenging. To overcome these limitations, we propose an alternative approach that computes repulsive forces directly between particle pairs. In fact, this strategy effectively preserves the characteristics of the microcone array. Through the implementation of parallel computing techniques, we maintain manageable computational costs while achieving significantly improved stability and broader applicability across various geometric configurations.

Let Γ denote the set of all microcone array points, as illustrated in Figure 3. The repulsive force exerted by a boundary particle at position $\mathbf{y} \in \Gamma$ on a fluid particle at position $\mathbf{x} \in \Omega$ is defined as

$$\mathbf{F}(\mathbf{x}, \mathbf{y}) = -p_{\text{rep}}(\mathbf{x}, \mathbf{y}) \nabla_{\mathbf{x}} W(\mathbf{x} - \mathbf{y}, R_2), \quad (15)$$

where R_2 represents the radius of repulsive interaction. The scalar function

$p_{\text{rep}}(\mathbf{x}, \mathbf{y})$, which we interpret as a pseudo-pressure term, takes the form

$$p_{\text{rep}}(\mathbf{x}, \mathbf{y}) = \tilde{\alpha} \rho(\mathbf{y}) \bar{v}_0^2 \left(1 - \frac{|\mathbf{x} - \mathbf{y}|}{h} \right). \quad (16)$$

The parameter $\tilde{\alpha}$ characterizes substrate properties and is adjustable, while \bar{v}_0 denotes the mean initial impact velocity of liquid droplets upon contact with the substrate. In this study, we set $\bar{v}_0 = 0.837$ m/s. Consequently, the total repulsive force acting on a fluid particle at position \mathbf{x} is obtained by integrating over all boundary particles as follows

$$\mathbf{F}(\mathbf{x}) = \int_{\Gamma} \mathbf{F}(\mathbf{x}, \mathbf{y}) d\mathbf{y} = - \int_{\Gamma} p_{\text{rep}}(\mathbf{x}, \mathbf{y}) \nabla_{\mathbf{x}} W(\mathbf{x} - \mathbf{y}, R_2) d\mathbf{y}. \quad (17)$$

We remark that p_{rep} shares the same physical dimensions as pressure p , justifying its interpretation as the pseudo-pressure at point \mathbf{x} induced by boundary point \mathbf{y} .

2.3 Governing equations with nonlocal interface and boundary interactions

With the interfacial tension–cohesion relationship quantified and repulsive forces expressed in a nonlocal form, we now integrate these formulations with the conservation laws of mass and momentum to derive the governing equations of the system:

$$\frac{d\rho}{dt} = -\rho \nabla \cdot \mathbf{u}, \quad (18)$$

$$\frac{d\mathbf{u}}{dt} = -\frac{\nabla p}{\rho} + \frac{\mu}{\rho} \nabla^2 \mathbf{u} + \mathbf{g} + \frac{4\sigma}{\rho^2 \varepsilon} \int_{\Omega} \rho(\mathbf{y}) \nabla_{\mathbf{x}} W(\mathbf{x} - \mathbf{y}, R_1) d\mathbf{y} \quad (19)$$

$$- \frac{1}{\rho} \int_{\Gamma} p_{\text{rep}}(\mathbf{x}, \mathbf{y}) \nabla_{\mathbf{x}} W(\mathbf{x} - \mathbf{y}, R_2) d\mathbf{y}, \quad (20)$$

$$\frac{d\mathbf{x}}{dt} = \mathbf{u}, \quad (21)$$

where the pressure p is determined by the equation of state

$$p = \frac{c^2 \rho_0}{\gamma} \left(\left(\frac{\rho}{\rho_0} \right)^{\gamma} - 1 \right). \quad (22)$$

3 Numerical Methods

3.1 Foundations of SPH Methodology

In the Smoothed Particle Hydrodynamics framework, the *kernel approximation* (also termed *integral approximation*) of a scalar field $f(\mathbf{x})$ is given by

$$f_I(\mathbf{x}) := \int_{\Omega} f(\mathbf{x}') W(\mathbf{x} - \mathbf{x}', h) d\mathbf{x}' \approx f(\mathbf{x}), \quad (23)$$

where W denotes the smoothing kernel function with support radius h . Introducing the normalized distance $q = |\mathbf{x} - \mathbf{y}|/(h/2)$, we consider two widely used kernel functions:

1). **Cubic Spline Kernel** [45]:

$$W^{\text{cs}}(\mathbf{x} - \mathbf{y}, h) = \tilde{W}^{\text{cs}}(q) = \begin{cases} \sigma_1 \left[1 - \frac{3}{2}q^2 \left(1 - \frac{q}{2} \right) \right], & 0 \leq q \leq 1, \\ \sigma_1(2 - q)^3/4, & 1 < q \leq 2, \\ 0, & q > 2, \end{cases} \quad (24)$$

where $\sigma_1 = [\pi(h/2)^3]^{-1}$ for three-dimension.

2). **Wendland Quintic Kernel** [46]:

$$W^{\text{wq}}(\mathbf{x} - \mathbf{y}, h) = \tilde{W}^{\text{wq}}(q) = \begin{cases} \sigma_2(1 - q/2)^4(2q + 1), & 0 \leq q \leq 2, \\ 0, & q > 2, \end{cases} \quad (25)$$

with $\sigma_2 = 21/[16\pi(h/2)^3]$ for three-dimension. The Wendland Quintic Kernel function can constitute a good choice in terms of computational accuracy and effectiveness, since it provides a higher order of interpolation with a computational cost comparable to the quadratic kernel.

Following the idea of Eq. (23), we can readily derive an approximation of the derivative function using integration by parts

$$[D^{\beta} f]_I(\mathbf{x}) = - \int_{\Omega} f(\mathbf{x}') D_{\mathbf{x}'}^{\beta} W(\mathbf{x} - \mathbf{x}', h) d\mathbf{x}', \quad (26)$$

where β denotes a multi-index characterizing the derivative order.

Discretization of the kernel approximation yields the *particle approximation* for both scalar fields and vector field divergences:

$$\langle f \rangle_i = \sum_j \frac{m_j}{\rho_j} f_j W_{ij}^{\text{wq}}, \quad (27)$$

$$\langle \nabla \cdot \mathbf{f} \rangle_i = - \sum_j \frac{m_j}{\rho_j} \mathbf{f}_j \cdot \nabla_j W_{ij}^{\text{wq}}, \quad (28)$$

where $f_j := f(\mathbf{x}_j)$, $W_{ij}^{\text{wq}} := W^{\text{wq}}(\mathbf{x}_i - \mathbf{x}_j, h)$ and $\nabla_j W_{ij}^{\text{wq}} := \nabla_{\mathbf{x}_j} W^{\text{wq}}(\mathbf{x}_i - \mathbf{x}_j, h)$. Here, i denotes the interpolating particle and j refers to the neighbouring particles within the support. $\frac{m_j}{\rho_j}$ represents the volume of the particle j .

In practical applications, modified versions of Eq. (28) are typically employed rather than their original forms. When a derivative function is multiplied or divided by density, it can be incorporated within the summation operator. Specifically, we consider the following two identities [45]:

$$[\rho \nabla \cdot \mathbf{f}](\mathbf{x}) = \nabla \cdot (\rho \mathbf{f})(\mathbf{x}) - \mathbf{f}(\mathbf{x}) \cdot \nabla \rho(\mathbf{x}), \quad (29)$$

$$\left[\frac{\nabla f}{\rho} \right] (\mathbf{x}) = \nabla \left(\frac{f}{\rho} \right) (\mathbf{x}) + \frac{f(\mathbf{x})}{\rho^2(\mathbf{x})} \nabla \rho(\mathbf{x}). \quad (30)$$

Combining Eq. (28), we obtain the following commonly used SPH formulas:

$$\langle \rho \nabla \cdot \mathbf{u} \rangle_i = - \sum_j m_j \mathbf{u}_{ij} \cdot \nabla_i W_{ij}^{\text{wq}}, \quad (31)$$

$$\left\langle \frac{\nabla p}{\rho} \right\rangle_i = \sum_j m_j \left(\frac{p_i}{\rho_i^2} + \frac{p_j}{\rho_j^2} \right) \nabla_i W_{ij}^{\text{wq}}. \quad (32)$$

Here, $\mathbf{u}_{ij} := \mathbf{u}_i - \mathbf{u}_j$. Another common SPH format is as follows

$$\left\langle \frac{\mu}{\rho} \nabla^2 \mathbf{u} \right\rangle_i = \sum_j \frac{m_j(\mu_i + \mu_j)}{(\rho_i + \rho_j)^2/4} \frac{\mathbf{x}_{ij} \cdot \nabla_i W_{ij}^{\text{wq}}}{|\mathbf{x}_{ij}|^2 + (0.01h_{ij})^2} \mathbf{u}_{ij}. \quad (33)$$

3.2 SPH formulations

While well-established SPH discretization schemes exist for local differential operators [47, 48, 49], this work focuses on developing novel formulations for non-local operators. The SPH framework demonstrates particular advantages for non-local operators due to its intrinsic non-local nature through kernel approximations. Specifically, we have

$$\begin{aligned} \left\langle \frac{\mathbf{f}_{\text{att}}}{\rho} \right\rangle_i &= \left\langle \frac{4\sigma}{\rho^2 \varepsilon} \int_{\Omega} \rho(\mathbf{y}) \nabla_{\mathbf{x}} W^{\text{cs}}(\mathbf{x} - \mathbf{y}, R_1) \, d\mathbf{y} \right\rangle_i \\ &:= \frac{4\sigma}{\rho_0^2 \varepsilon} \sum_{j=1}^{N_f} m_j \nabla_i W_{ij}^{\text{cs}, R_1}, \end{aligned} \quad (34)$$

and

$$\begin{aligned} \left\langle \frac{\mathbf{F}}{\rho} \right\rangle_i &= \left\langle -\frac{1}{\rho} \int_{\Gamma} p_{\text{rep}}(\mathbf{x}, \mathbf{y}) \nabla_{\mathbf{x}} W^{\text{wq}}(\mathbf{x} - \mathbf{y}, R_2) d\mathbf{y} \right\rangle_i \\ &:= -\tilde{\alpha} \rho_0 \bar{v}_0^2 \sum_{k=1}^{N_s} \frac{m_k}{\rho_i \rho_k} \left(1 - \frac{|\mathbf{x}_{ik}|}{R_2} \right) \nabla_i W_{ik}^{\text{wq}, R_2}, \end{aligned} \quad (35)$$

where $\nabla_i W_{ij}^{\text{cs}, R_1} := \nabla_{\mathbf{x}_i} W^{\text{cs}}(\mathbf{x}_i - \mathbf{x}_j, R_1)$ and $\nabla_i W_{ij}^{\text{wq}, R_2} := \nabla_{\mathbf{x}_i} W^{\text{wq}}(\mathbf{x}_i - \mathbf{x}_j, R_2)$.

Then the governing equations can be rewritten as follows. Let N_f denote the number of fluid particles and N_s denote the number of solid particles. For any $1 \leq i, j \leq N_f$, $1 \leq k \leq N_s$, we solve the following system

$$\frac{d\rho_i}{dt} = \sum_{j=1}^{N_f + N_s} m_j \mathbf{u}_{ij} \cdot \nabla_i W_{ij}^{\text{wq}}, \quad p_i = \frac{c^2 \rho_0}{\gamma} \left(\left(\frac{\rho_i}{\rho_0} \right)^\gamma - 1 \right), \quad (36)$$

$$\begin{aligned} \frac{d\mathbf{u}_i}{dt} &= - \sum_{j=1}^{N_f} m_j \left(\frac{p_i}{\rho_i^2} + \frac{p_j}{\rho_j^2} + \Pi_{i,j}^{\text{art}} \right) \nabla_i W_{ij}^{\text{wq}} + \frac{4\sigma}{\varepsilon \rho_0^2} \sum_{j=1}^{N_f} m_j \nabla_i W_{ij}^{\text{cs}, R_1} \\ &\quad - \sum_{k=1}^{N_s} m_k \left(\frac{\tilde{\alpha} \rho_0 \bar{v}_0^2}{\rho_k \rho_i} \frac{R_2 - |\mathbf{x}_{ik}|}{R_2} + \Pi_{i,k}^{\text{art}} \right) \nabla_i W_{ik}^{\text{wq}, R_2} \\ &\quad + \sum_{j=1}^{N_f} \frac{m_j (\mu_i + \mu_j)}{(\rho_i + \rho_j)^2 / 4} \frac{\mathbf{x}_{ij} \cdot \nabla_i W_{ij}^{\text{wq}}}{|\mathbf{x}_{ij}|^2 + 0.01(h_{ij})^2} \mathbf{u}_{ij} + \mathbf{g}_i, \end{aligned} \quad (37)$$

$$\frac{d\mathbf{x}_i}{dt} = (1 - \epsilon) \mathbf{u}_i + \epsilon \sum_{j=1}^{N_f} m_j \mathbf{u}_{ij} W_{ij}^{\text{wq}}. \quad (38)$$

Here, $\Pi_{a,b}^{\text{art}}$ is artificial viscosity term proposed by Monaghan [47] and

$$\Pi_{a,b}^{\text{art}} = \begin{cases} \frac{-\alpha c \mu_{ab}}{\bar{\rho}_{ab}} & \mathbf{u}_{ab} \cdot \mathbf{x}_{ab} < 0; \\ 0 & \mathbf{u}_{ab} \cdot \mathbf{x}_{ab} \geq 0; \end{cases}, \quad \mu_{ab} = \frac{h \mathbf{u}_{ab} \cdot \mathbf{x}_{ab}}{\mathbf{x}_{ab}^2 + 0.01h^2}, \quad \bar{\rho}_{ab} = \frac{\rho_a + \rho_b}{2}. \quad (39)$$

We set $\epsilon = 0.5$ [44] and $\alpha = 0.015$ to guarantee the stability of the numerical scheme.

3.3 Time integration

The Predict-Evaluate-Correct (PEC) method is adopted for time integration, offering high computational efficiency and minimal storage demands. For each time step, one can get ρ_i^{n+1} , \mathbf{u}_i^{n+1} , \mathbf{x}_i^{n+1} , $\frac{d\rho_i^{n+1/2}}{dt}$, $\frac{d\mathbf{u}_i^{n+1/2}}{dt}$, $\frac{d\mathbf{x}_i^{n+1/2}}{dt}$ by given ρ_i^n , \mathbf{u}_i^n , \mathbf{x}_i^n , $\frac{d\rho_i^{n-1/2}}{dt}$, $\frac{d\mathbf{u}_i^{n-1/2}}{dt}$, $\frac{d\mathbf{x}_i^{n-1/2}}{dt}$. Firstly, we predict the value at time $t = t_{n+\frac{1}{2}}$ by

$$\begin{cases} \rho_i^{n+1/2} = \rho_i^n + \frac{\Delta t}{2} \cdot \frac{d\rho_i^{n-1/2}}{dt}, \\ \mathbf{u}_i^{n+1/2} = \mathbf{u}_i^n + \frac{\Delta t}{2} \cdot \frac{d\mathbf{u}_i^{n-1/2}}{dt}, \\ \mathbf{x}_i^{n+1/2} = \mathbf{x}_i^n + \frac{\Delta t}{2} \cdot \frac{d\mathbf{x}_i^{n-1/2}}{dt}, \end{cases} \quad (40)$$

where Δt is the given time step. Secondly, we evaluate the derivative value at time $t = t_{n+\frac{1}{2}}$ by

$$\begin{cases} \frac{d\rho_i^{n+1/2}}{dt} = \frac{d\rho_i}{dt}(\rho_i^{n+1/2}, \mathbf{u}_i^{n+1/2}, \mathbf{x}_i^{n+1/2}), \\ \frac{d\mathbf{u}_i^{n+1/2}}{dt} = \frac{d\mathbf{u}_i}{dt}(\rho_i^{n+1/2}, \mathbf{u}_i^{n+1/2}, \mathbf{x}_i^{n+1/2}), \\ \frac{d\mathbf{x}_i^{n+1/2}}{dt} = \frac{d\mathbf{x}_i}{dt}(\rho_i^{n+1/2}, \mathbf{u}_i^{n+1/2}, \mathbf{x}_i^{n+1/2}). \end{cases} \quad (41)$$

Finally, we can correct the value by

$$\begin{cases} \rho_i^{n+1} = \rho_i^n + \Delta t \cdot \frac{d\rho_i^{n+1/2}}{dt}, \\ \mathbf{u}_i^{n+1} = \mathbf{u}_i^n + \Delta t \cdot \frac{d\mathbf{u}_i^{n+1/2}}{dt}, \\ \mathbf{x}_i^{n+1} = \mathbf{x}_i^n + \Delta t \cdot \frac{d\mathbf{x}_i^{n+1/2}}{dt}. \end{cases} \quad (42)$$

This PEC scheme ensures second-order accuracy in time while maintaining numerical stability, making it particularly suitable for long-time simulations in particle-based methods.

4 Numerical Validation

This section presents systematic validation of the proposed SPH framework through comprehensive simulations of droplet impact dynamics on superhydrophobic microcone arrays. The study examines a range of Weber numbers (We), defined as:

$$We = \frac{\rho v_0^2 r_0}{\sigma}, \quad (43)$$

where $\rho = 1 \text{ g/cm}^3$ represents the water density and $\sigma = 0.0728 \text{ N/m}$ denotes the surface tension coefficient. The fluid properties include dynamic viscosity $\mu = 10^{-3} \text{ Pa} \cdot \text{s}$ ($10^{-6} \text{ g}/(\text{mm} \cdot \text{ms})$) and gravitational acceleration $\mathbf{g} = 9.81 \text{ m/s}^2$. Quantitative validation against the experimental data of [8] (see Supplementary Movies 1–3 in their original work, available at: <https://www.nature.com/articles/nphys2980#Sec7>) confirms the accuracy of our numerical framework. For direct comparison, the corresponding simulations are provided in Supplementary Movies 1–3, showing consistent spatiotemporal patterns with the experiments.

4.1 Geometric Configuration

The microcone array exhibits the following dimensional characteristics:

- Cone height: $H = 0.8 \text{ mm}$
- Base radius: $R_{\max} = 0.045 \text{ mm}$
- Tip radius: $R_{\min} = 0.01 \text{ mm}$

Arranged in a chessboard pattern with center-to-center spacing $L = 0.2 \text{ mm}$, the microcones form a complex structured surface with high curvature gradients. The impacting water droplet has initial radius $r_0 = 1.45 \text{ mm}$, with impact velocity v_0 determined by the target Weber number via Eq. (43). Figure 1 shows the initial computational domain configuration, including the droplet’s initial position relative to the micro-structured surface.

4.2 Computational Parameters

The SPH simulation utilizes carefully selected parameters to balance numerical accuracy with computational efficiency. We set the initial particle spacing to $\Delta x = 0.06 \text{ mm}$, providing sufficient resolution to capture detailed droplet dynamics. The thickness of the surface is set as $\varepsilon = 0.06 \text{ mm}$. For the kernel function implementation, we employ two distinct characteristic length scales: (1) an interaction radius of $R_1 = 0.26 \text{ mm}$ for cohesion simulation, and (2) a smoothing length of $h = R_2 = 0.1625 \text{ mm}$ for field variable calculations and repulsive force modeling. The numerical speed of sound is set to $c = 10(1 \text{ m/s} + v_0)$, and the time step is dynamically adjusted as $\Delta t = 0.062R_1/c$ to maintain numerical stability. The model incorporates

only one adjustable parameter, the dimensionless substrate parameter $\tilde{\alpha}$, which takes fixed values of 57 (horizontal placement) and 38.73 (tilted configuration). Crucially, for horizontal surfaces, $\tilde{\alpha}$ maintains a constant value regardless of Weber number changes, and its single-parameter nature enables easy determination through simple calibration.

4.3 Droplet Bouncing on Horizontal Microcone Arrays

4.3.1 Case 1: Low-Weber-Number Impact ($We = 7.1$)

The experimental setup consists of a water droplet with diameter r_0 impacting the microcone array at velocity $v_0 = 0.594$ m/s. Snapshots of the numerical simulations are presented in Figure 4 and compared to the experiment. Experimental observations reveal that under low Weber number conditions, droplets exhibit conventional bouncing behavior on micro-cone arrays, characterized by contraction prior to detachment from the substrate. The numerical simulations (Supplementary Movie 1) demonstrate remarkable temporal consistency with physical experiments throughout the entire process. Figure 5 presents the temporal evolution of the droplet's horizontal diameter and its vertical height relative to the substrate during the bouncing process. We define t_{\uparrow} as the time instant when the droplet vertical height first reaches zero, and t_{contact} as the moment when the droplet height first attains $3h$. A distinct downward impact is observed around $t = 10$ ms, consistent with experimental observations. This impact, in fact, provides the droplet with sufficient momentum to detach from the substrate.

4.3.2 Case 2: Moderate-Weber-Number Impact ($We = 14.1$)

At higher impact energy ($v_0 = 0.837$ m/s), the droplet exhibits more complex dynamics. As illustrated in Figure 6, the droplet deviates from conventional bouncing behavior and exhibits a counterintuitive sequence: detachment from the substrate occurs prior to maximum spreading. The close agreement between numerical snapshots and experimental observations demonstrates the remarkable simulation capability of the proposed method. Furthermore, Figure 7 presents the temporal variations of droplet radius and vertical height obtained from numerical simulations (Supplementary Movie 2). A clear sequence is observed: after detaching from the substrate, the droplet continues to spread until reaching its maximum radius before subsequent contraction.

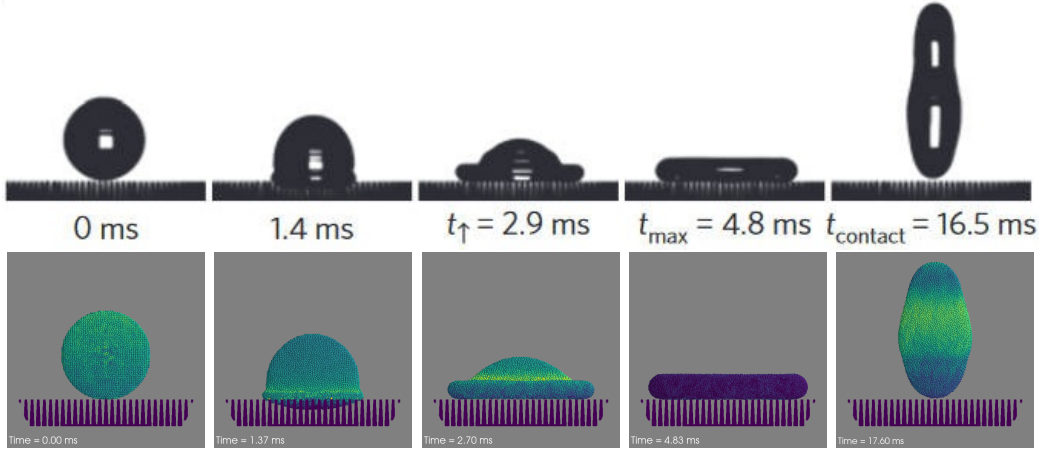


Figure 4: Comparison of simulated (bottom) and experimental (top; Copyright 2014 Springer Nature) droplet shapes during droplet bouncing at $We = 7.1$. Time instances show initial impact at $t = 0$ ms, maximal spreading at $t = 4.8$ ms, and complete rebound at $t = 16.5$ ms.

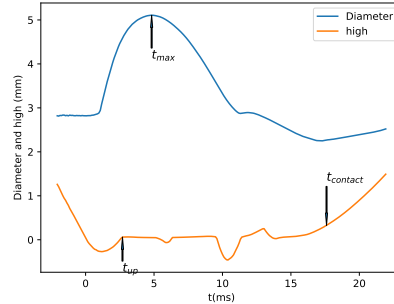


Figure 5: Diameter and height of droplet with $We = 7.1$

4.4 Dynamic Evolution Analysis ($We \in [7, 24]$)

To further validate the universality of the present method, we conducted simulations of droplet bouncing across a Weber number range of 7 to 24 and systematically compared the results with experimental data. To quantita-

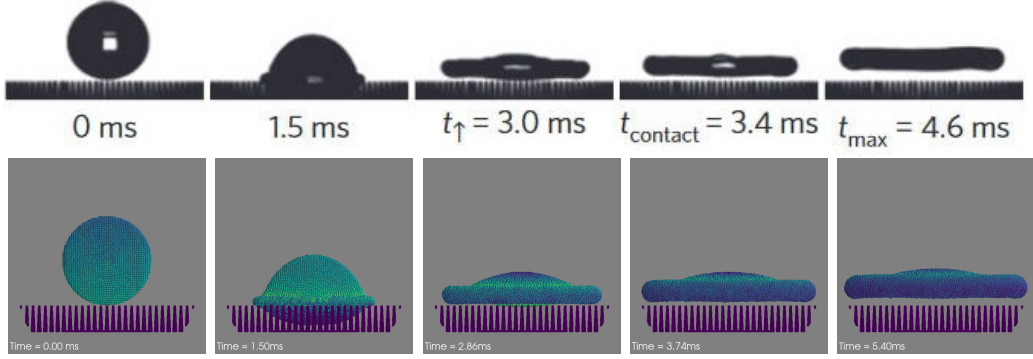


Figure 6: Comparison of simulated (bottom) and experimental (top; Copyright 2014 Springer Nature) droplet shapes during droplet bouncing at $We = 14.1$. Time instances show initial impact at $t = 0$ ms, complete rebound at $t = 3.4$ ms and maximal spreading at $t = 4.6$ ms.

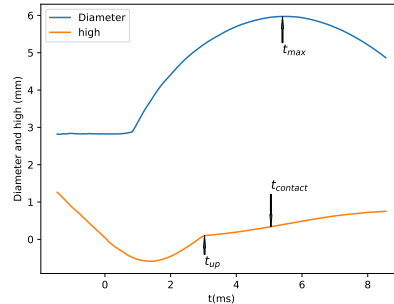


Figure 7: Diameter and height of droplet with $We = 14.1$

tively assess the pancake effect, we introduce pancake quality as

$$Q = \frac{d_{\text{jump}}}{d_{\text{max}}}, \quad (44)$$

where d_{jump} is the droplet diameter at detachment time t_{contact} and d_{max} represents the global maximum diameter during spreading. As illustrated in Figure 8, the numerical results of pancake quality exhibit excellent agreement with experimental measurements. Figure 8 also shows the temporal

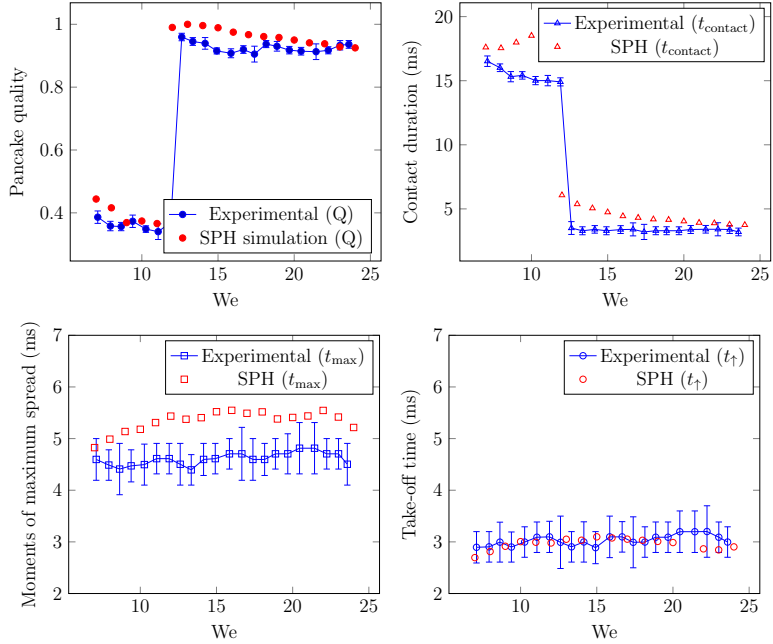


Figure 8: Comparison of droplet dynamics between SPH simulations and experimental measurements [8]. Error bars represent standard deviations from experimental repetitions.

characteristics under different Weber numbers, including the detachment time, maximum spreading time and take-off time along with their experimental counterparts. The comparison demonstrates satisfactory consistency between numerical predictions and physical observations.

4.5 Oblique bouncing on tilted substrates ($We = 31.2$, $\theta = 30^\circ$)

One practical application of superhydrophobic microcone arrays is in the development of anti-icing materials. In real-world scenarios, droplets typically impact the surface at an oblique angle rather than perpendicularly. To accurately simulate this physical phenomenon, we investigate the bouncing dynamics of water droplets on an inclined substrate. Specifically, the array plane is tilted at 30 degrees while maintaining vertical droplet impact. The simulation results are presented in Figure 9, with experimental and numer-

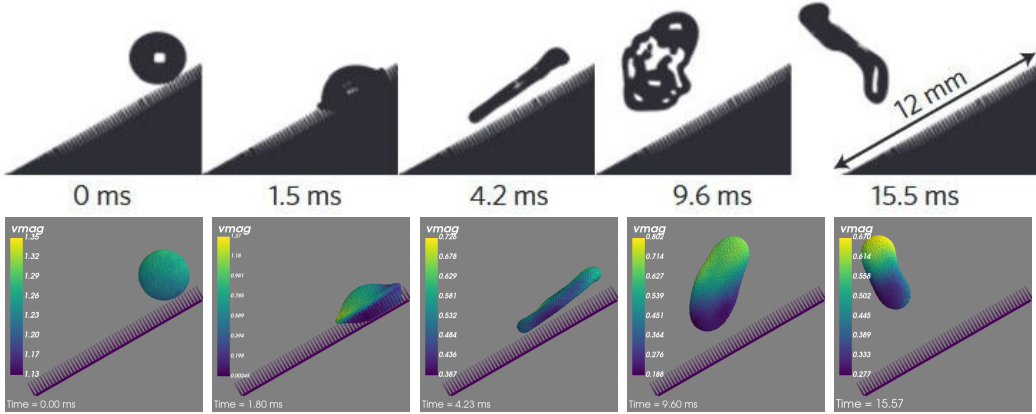


Figure 9: Comparative analysis of experimental (top; Copyright 2014 Springer Nature) and simulated (bottom) droplet morphologies at $We=31.2$ (velocity magnitude shown in color scale)

ical results shown in the top and bottom panels, respectively. Notably, the droplet detaches from the substrate in a pancake-like shape (Supplementary Movie 3), demonstrating well agreement with experimental observations.

4.6 Secondary droplets formed by the Worthington jet ($We = 14.1$)

Droplets with moderate Weber numbers have the potential to undergo secondary impacts subsequent to their initial interaction with the substrate. This secondary impact is often more forceful, imparting sufficient momentum to the droplet for it to rebound to a greater height and produce satellite droplets – a phenomenon extensively documented in prior research [50, 51]. To assess the ability of our model to capture subsequent droplet dynamics, we conducted extended numerical simulations for a droplet with $We=14.1$ (Supplementary Movie 2). As depicted in Figure 10, the numerical outcomes effectively replicate the entire sequence of events: secondary impact, jet formation, and eventual satellite droplet generation. These findings underscore the reliability of the proposed contact algorithm and the precision of the cohesion model integrated in this investigation.

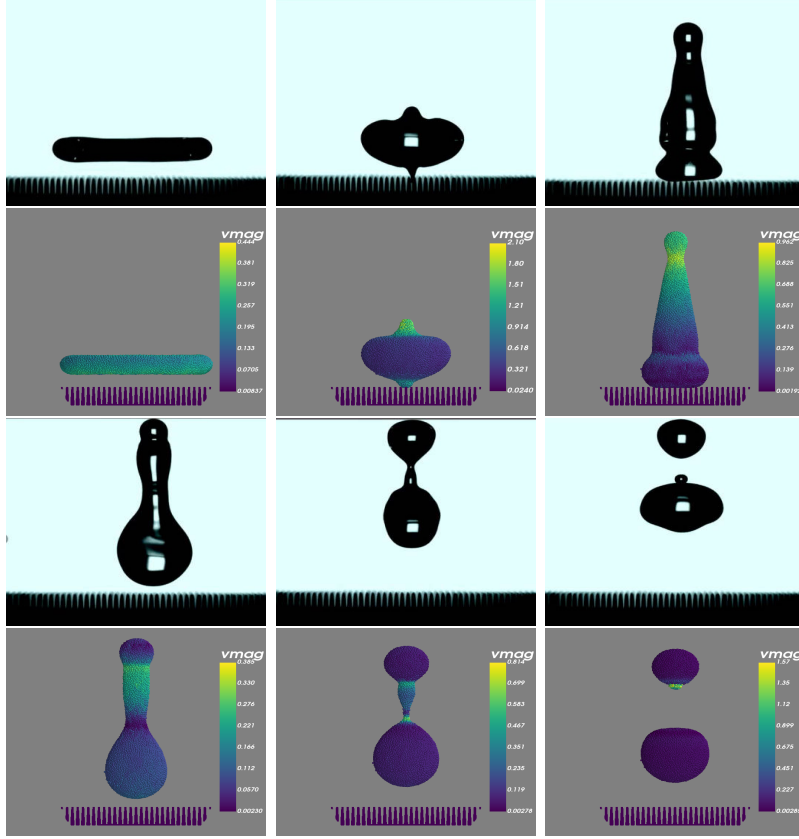


Figure 10: Secondary droplet formation at $We=14.1$ (top/third rows: experiment, Copyright 2014 Springer Nature; second/fourth rows: simulation, velocity magnitude in color scale)

5 Conclusions

This study presents a rigorously derived nonlocal SPH framework for simulating 3D pancake bouncing dynamics on superhydrophobic microcone arrays. By formulating intermolecular forces to model surface tension through strict theoretical derivations—linking microscopic interactions to the macroscopic surface tension coefficient—we eliminate empirical parameter dependencies. Additionally, the proposed nonlocal contact repulsion mechanism resolves fundamental challenges in defining local normals on irregular microstructures, ensuring numerical stability for high-Weber-number impacts. These advances provide a mathematically grounded perspective for SPH-based modeling of

complex droplet-substrate interactions, significantly expanding the method's capability to capture microstructure-driven phenomena. Numerical validations demonstrate excellent agreement with experimental data, underscoring the model's accuracy in predicting droplet dynamics. The framework's versatility opens avenues for applications requiring precise droplet control, such as anti-icing surfaces and microfluidic systems. Future work will extend this methodology to dynamic wetting scenarios and multi-droplet interactions, further addressing open questions in interfacial flows while leveraging the nonlocal formulations developed here.

Funding

This work is supported by the CAS AMSS-PolyU Joint Laboratory of Applied Mathematics (No. JLFS/P-501/24). The first author was partially supported by the Hong Kong Research Grants Council RFS grant RFS2021-5S03 and GRF grant 15305624. The third author was partially supported by the Hong Kong Polytechnic University Postdoctoral Research Fund 1-W30N.

Declaration of interests

The authors report no conflict of interest.

A Derivation of Equations (12) and (13)

Proof 2 *We begin by defining the integral functional:*

$$G_f := \int_0^{R_1} \int_0^\pi \int_0^{\arccos(s/R_1)} \int_{s/\cos\theta}^{R_1} f(r) \cos\theta r^2 \sin\theta dr d\theta d\phi ds.$$

The integral simplifies in three steps. First, integrating over ϕ yields:

$$G_f = \pi \int_0^{R_1} \int_0^{\arccos(s/R_1)} \cos\theta \sin\theta \int_{s/\cos\theta}^{R_1} f(r) r^2 dr d\theta ds. \quad (45)$$

Next, applying the substitution $u = s/R_1$ transforms (45) to:

$$G_f = \pi R_1 \int_0^1 \int_0^{\arccos u} \cos\theta \sin\theta \int_{R_1 u/\cos\theta}^{R_1} f(r) r^2 dr d\theta du.$$

We then exchange the integration order of u and θ :

$$G_f = \pi R_1 \int_0^{\pi/2} \cos \theta \sin \theta \int_0^{\cos \theta} \int_{R_1 u / \cos \theta}^{R_1} f(r) r^2 dr du d\theta.$$

A second exchange of integration order gives:

$$\begin{aligned} G_f &= \pi R_1 \int_0^{\pi/2} \cos \theta \sin \theta \int_0^{R_1} f(r) r^2 \int_0^{r \cos \theta / R_1} du dr d\theta \\ &= \pi \int_0^{\pi/2} \cos^2 \theta \sin \theta d\theta \int_0^{R_1} f(r) r^3 dr \\ &= \frac{\pi}{3} \int_0^{R_1} f(r) r^3 dr, \end{aligned} \tag{46}$$

where we have used $\int_0^{\pi/2} \cos^2 \theta \sin \theta d\theta = \frac{1}{3}$.

For the special case where $f(|\mathbf{x}|) = \partial_{|\mathbf{x}|} W(\mathbf{x}, h)$ with W being a kernel function, we proceed as follows. The normalization condition requires:

$$1 = \int W(\mathbf{x}, R_1) d\mathbf{x} = 4\pi \int_0^{R_1} \tilde{W}(r) r^2 dr, \tag{47}$$

where $\tilde{W}(|\mathbf{x}|) = W(\mathbf{x}, h)$.

Evaluating (46) through integration by parts:

$$\begin{aligned} G_f &= \frac{\pi}{3} \int_0^{R_1} \partial_r \tilde{W}(r) r^3 dr \\ &= \frac{\pi}{3} \left[r^3 \tilde{W}(r) \Big|_0^{R_1} - 3 \int_0^{R_1} \tilde{W}(r) r^2 dr \right] \\ &= -\pi \int_0^{R_1} \tilde{W}(r) r^2 dr. \end{aligned} \tag{48}$$

Combining (47) with (48) establishes:

$$G_f = -\frac{1}{4}.$$

References

[1] W. A Sirignano. Advances in droplet array combustion theory and modeling. *Prog. Energy Combust. Sci.*, 42:54–86, 2014.

- [2] H. Wijshoff. Drop dynamics in the inkjet printing process. *Cur. Opin. Colloid Interface Sci.*, 36:20–27, 2018.
- [3] J. C Bird, R. Dhiman, H.-M. Kwon, and K. K Varanasi. Reducing the contact time of a bouncing drop. *Nature*, 503(7476):385–388, 2013.
- [4] D. Zhang, L. Wang, H. Qian, and X. Li. Superhydrophobic surfaces for corrosion protection: a review of recent progresses and future directions. *J. Coat. Technol. Res.*, 13:11–29, 2016.
- [5] R. Blossey. Self-cleaning surfaces-virtual realities. *Nat. Mater*, 2(5):301–306, 2003.
- [6] M. Zaman Khan, J. Militky, M. Petru, B. Tomková, A. Ali, E. Tören, and S. Perveen. Recent advances in superhydrophobic surfaces for practical applications: A review. *Eur. Polym. J.*, 178:111481, 2022.
- [7] A. Nakajima. Design of hydrophobic surfaces for liquid droplet control. *NPG Asia Mater.*, 3(5):49–56, 2011.
- [8] Y. Liu, L. Moevius, X. Xu, T. Qian, J. M Yeomans, and Z. Wang. Pancake bouncing on superhydrophobic surfaces. *Nat. Phys.*, 10(7):515–519, 2014.
- [9] Alireza Mohammad K. Physics of droplet impact on various substrates and its current advancements in interfacial science: A review. *J. Appl. Phys.*, 133(3), 2023.
- [10] T. M Schutzius, S. Jung, T. Maitra, G. Graeber, M. Köhme, and D. Poulikakos. Spontaneous droplet trampolining on rigid superhydrophobic surfaces. *Nature*, 527(7576):82–85, 2015.
- [11] C. Hao, J. Li, Y. Liu, X. Zhou, Y. Liu, R. Liu, L. Che, W. Zhou, D. Sun, L. Li, et al. Superhydrophobic-like tunable droplet bouncing on slippery liquid interfaces. *Nat. Commun.*, 6(1):7986, 2015.
- [12] Y. Liu and Z. Wang. Superhydrophobic porous networks for enhanced droplet shedding. *Sci. Rep.*, 6(1):33817, 2016.
- [13] S. Yun. Bouncing of an ellipsoidal drop on a superhydrophobic surface. *Sci. Rep.*, 7(1):17699, 2017.

- [14] S. Zhao, Z. Ma, M. Song, L. Tan, H. Zhao, and L. Ren. Golden section criterion to achieve droplet trampoline effect on metal-based superhydrophobic surface. *Nat. Commun.*, 14(1):6572, 2023.
- [15] W. Fang, S. Wang, H. Duan, S. A. Tahir, K. Zhang, L. Wang, X.-Q. Feng, and M. Song. Target slinging of droplets with a flexible cantilever. *Droplet*, 2(3):e72, 2023.
- [16] R. Lathia, C. D Modak, and P. Sen. Two modes of contact-time reduction in the impact of particle-coated droplets on superhydrophobic surfaces. *Droplet*, 2(4):e89, 2023.
- [17] V. Kumar, Q. Fu, H. Szeto, and Y. Zhu. Heat transfer during droplet impact on a cold superhydrophobic surface via interfacial thermal mapping. *Droplet*, 3(3):e124, 2024.
- [18] A. Goswami and Y. Hardalupas. Simultaneous impact of droplet pairs on solid surfaces. *J. Fluid Mech.*, 961:A17, 2023.
- [19] C. Yue, Q. Dai, X. Yang, C. Gachot, W. Huang, and X. Wang. Controllable self-transport of bouncing droplets on ultraslippery surfaces with wedge-shaped grooves. *Droplet*, 3(2):e118, 2024.
- [20] W. Qian, W. Zhao, T. Qian, and Q. Xu. Emergence and growth dynamics of wetting-induced phase separation on soft solids. *Phys. Rev. Res.*, 6(3):033210, 2024.
- [21] B. Sobac, A. Rednikov, and P. Colinet. Small Leidenfrost droplet dynamics. *J. Fluid Mech.*, 1010:A47, 2025.
- [22] D. Khojasteh, M. Kazerooni, S. Salarian, and R. Kamali. Droplet impact on superhydrophobic surfaces: A review of recent developments. *J. Ind. Eng. Chem.*, 42:1–14, 2016.
- [23] F. Huang, W. Bao, and T. Qian. Phase-field simulations for dripping-to-jetting transitions: Effects of low interfacial tension and bulk diffusion. *Phys. Fluids*, 35(7), 2023.
- [24] C. Zhang, J. Li, L.-S. Luo, and T. Qian. Numerical simulation for a rising bubble interacting with a solid wall: Impact, bounce, and thin film dynamics. *Phys. Fluids*, 30(11), 2018.

- [25] S. Ray, Y. Han, Z. Yue, H. Guo, C. Chao, and S. Cheng. New insights into head-on bouncing of unequal-size droplets on a wetting surface. *J. Fluid Mech.*, 983:A25, 2024.
- [26] Z. Qiao, X. Yang, and Y. Zhang. Thermodynamic-consistent multiple-relaxation-time lattice boltzmann equation model for two-phase hydrocarbon fluids with Peng-Robinson equation of state. *Int. J. Heat Mass Transfer*, 141:1216–1226, 2019.
- [27] Z. Qiao, X. Yang, and Y. Zhang. A free-energy based multiple-distribution-function Lattice Boltzmann method for multi-component and multi-phase flows. *Appl. Therm. Eng.*, 257:124241, 2024.
- [28] W. Zhang, S. Kuang, Z. Chai, and B. Shi. Thirteen-Velocity three-dimensional multiple-relaxation-time Lattice Boltzmann model for incompressible Navier-Stokes equations. *Adv. Appl. Math. Mech.*, 17(4):1037–1062, 2025.
- [29] J. King, S. Lind, B. Rogers, P. Stansby, and R. Vacondio. Large eddy simulations of bubbly flows and breaking waves with smoothed particle hydrodynamics. *J. Fluid Mech.*, 972:A24, 2023.
- [30] Q. Du and X. Tian. Mathematics of Smoothed Particle Hydrodynamics: A study via nonlocal Stokes equations. *Found. Comput. Math.*, 20(4):801–826, 2020.
- [31] H. Lee and Q. Du. Asymptotically compatible SPH-like particle discretizations of one dimensional linear advection models. *SIAM J. Numer. Anal.*, 57(1):127–147, 2019.
- [32] X. Feng, Z. Qiao, S. Sun, and X. Wang. An energy-stable Smoothed Particle Hydrodynamics discretization of the Navier-Stokes-Cahn-Hilliard model for incompressible two-phase flows. *J. Comput. Phys.*, 479:111997, 2023.
- [33] X. Zhu, S. Sun, and J. Kou. An energy stable SPH method for incompressible fluid flow. *Adv. Appl. Math. Mech.*, 14(5):1201–1224, 2022.
- [34] X. Zhu, X. Wang, J. Kou, and S. Sun. An energy stable incompressible SPH method with consistent solid boundary treatment. *J. Comput. Appl. Math.*, 436:115367, 2024.

- [35] J. U Brackbill, D. B Kothe, and C. Zemach. A continuum method for modeling surface tension. *J. Comput. Phys.*, 100(2):335–354, 1992.
- [36] Y. Huo, Y. Zhong, M. Xin, and S. Li. Modeling and simulation of droplet impact on an elastic beam based on FEM-SPH and SPH-SPH FSI methods. *Ocean Eng.*, 310:118730, 2024.
- [37] X. Dong, Y. Liu, R. Yu, and M. Fan. Simulation of droplet bouncing on flexible substrate in 2d and 3d with WC-TL SPH method. *J. Fluids Struct.*, 119:103864, 2023.
- [38] M. Blank, P. Nair, and T. Pöschel. Surface tension and wetting at free surfaces in smoothed particle hydrodynamics. *J. Fluid Mech.*, 987:A23, 2024.
- [39] A. Tartakovsky and P. Meakin. Modeling of surface tension and contact angles with smoothed particle hydrodynamics. *Phys. Rev. E*, 72(2):026301, 2005.
- [40] T. Breinlinger, P. Polfer, A. Hashibon, and T. Kraft. Surface tension and wetting effects with smoothed particle hydrodynamics. *J. Comput. Phys.*, 243:14–27, 2013.
- [41] X. Dong, L. Feng, and Q. Zhang. Droplet asymmetry bouncing on structured surfaces: A simulation based on SPH method. *Int. J. Adhes. Adhes.*, 132:103734, 2024.
- [42] K.-L. Pan, P.-C. Chou, and Y.-J. Tseng. Binary droplet collision at high weber number. *Phys. Rev. E*, 80(3):036301, 2009.
- [43] X. Dong, X. Huang, and J. Liu. Modeling and simulation of droplet impact on elastic beams based on SPH. *Eur. J. Mech. A-Solids*, 75:237–257, 2019.
- [44] J. J Monaghan. Simulating free surface flows with SPH. *J. Comput. Phys.*, 110(2):399–406, 1994.
- [45] J. J Monaghan. Smoothed Particle Hydrodynamics. *Annu. Rev. Astron. Astrophys.*, 30:543–574, 1992.

- [46] M. Gomez-Gesteira, B. D Rogers, R. A Dalrymple, and A. JC Crespo. State-of-the-art of classical SPH for free-surface flows. *J. Hydraul. Res.*, 48(sup1):6–27, 2010.
- [47] J. J Monaghan. Smoothed particle hydrodynamics. *Rep. Prog. Phys.*, 68(8):1703, 2005.
- [48] G.-R. Liu and M. Liu. *Smoothed particle hydrodynamics: a meshfree particle method*. World scientific, 2003.
- [49] M. Liu and G.-R. Liu. Smoothed Particle Hydrodynamics (SPH): an overview and recent developments. *Arch. Comput. Methods Eng.*, 17(1):25–76, MAR 2010.
- [50] A. I Aria and M. Gharib. Physicochemical characteristics and droplet impact dynamics of superhydrophobic carbon nanotube arrays. *Langmuir*, 30(23):6780–6790, 2014.
- [51] B. Zhang, V. Sanjay, S. Shi, Y. Zhao, C. Lv, X.-Q. Feng, and D. Lohse. Impact forces of water drops falling on superhydrophobic surfaces. *Phys. Rev. Lett.*, 129(10):104501, 2022.